

High-Load Capable Soft Tactile Sensors: Incorporating Magnetorheological Elastomer for Accurate Contact Detection and Classification of Asymmetric Mechanical Components

Buyong Lim and Jungwon Yoon*

Soft tactile sensors are soft and sufficiently flexible for attachment to a robot's gripper to enhance human-like sensory capabilities. However, existing tactile sensors exhibit large size and a limited force measurement range. This article presents a novel design of a new soft tactile sensor for a robotic gripper, incorporating a sandwich-like multilayered structure, together with a deep learning (DL) model, which overcomes the limitations of traditional sensors. The structure consists of three distinct layers: a 15 wt% iron magnetorheological elastomer, a flexible printable circuit board layer equipped with three-dimensional Hall sensors (TLE493D; Infineon), and permanent magnets. Additionally, a multilayer perceptron network that can classify the loading state is adopted for the DL model. This new tactile sensor is capable of performing three distinct functions simultaneously: measurement of normal forces up to 3.73 kgf, identification of the precise location of force occurrence by subdivision into intervals of 2.5 mm, and differentiation between a wide (≈ 8 mm) and narrow (≈ 2 mm) contacted surface area. This newly developed soft tactile sensor has considerable potential for improvement in the performance of robotic grippers through its high accuracy, resolution, and large measurement range, as demonstrated by experimentation with the sensor attached to a real gripper.

vegetables, and mechanical components with human-like sensory capabilities.^[2,3]

A variety of sensor types are currently emerging, with differing purposes and environments in mind. For the measurement of human physical activity, sensors can be fabricated as thin films,^[4,5] or even foam if they require very soft properties.^[6] Among these diverse soft sensor mechanisms, optical, capacitance, and magnet-based systems have gained particular attention as force measurement systems. Optical sensors utilize a camera to monitor pressure-related changes in the skin surface.^[7,8] These sensors typically consist of a wide-angle camera placed inside a soft gripper, which has a thin hemispherical skin with visual markers attached. The camera captures images to analyze skin deformation as the gripper grasps the object, determining its shape and contact force. These systems are highly accurate, with excellent resolution, rapid response times, and low sensitivity to electromagnetic interference. However, their sensor

bulkiness is a limiting factor since the camera must be thick enough to provide a good overall view of the skin. For instance, ref. [9] notes limitations in thickness (≈ 30 mm), measuring area (13×17 mm²), and force measurement range (≈ 1.4 N).


Capacitance-based sensors detect external forces by measuring changes in capacitance. They typically consist of an array of channels where metal channels intersect with each other.^[10–12] These sensors can be easily fabricated from elastomers and metals, making them suitable for integration into most pneumatic soft grippers. However, capacitance-based sensors typically have limitations such as a limited force measurement range, low force resolution,^[13,14] signal drift, and limited stretchability.^[10]

Magnet-based sensors, especially those utilizing magnetic sources and Hall sensors, can be designed to be slim. They are capable of detecting both the strength and location of externally applied normal and shear forces.^[15–19] Bhirangi et al.^[20] introduced a soft tactile sensor that utilizes Hall sensors to measure normal and shear forces. The sensor exploits the motion and distortion of a magnetized film in a specific pattern. A deep learning (DL) neural network is used to determine the location of the applied force. However, the sensor's maximum measurable

1. Introduction

Soft tactile sensors are crucial in modern robotics, where the primary objective is to enable robots to perform proper grasping and locomotion in unstructured environments while cooperating with humans.^[1] For this purpose, a soft tactile sensor attached to the gripper can provide tactile feedback to the robot, enabling robots to grasp objects such as fruits,

B. Lim, J. Yoon
School of Integrated Technology
Gwangju Institute of Science and Technology
Gwangju 61005, Republic of Korea
E-mail: jyoon@gist.ac.kr

 The ORCID identification number(s) for the author(s) of this article can be found under <https://doi.org/10.1002/aisy.202400275>.

© 2024 The Author(s). Advanced Intelligent Systems published by Wiley-VCH GmbH. This is an open access article under the terms of the Creative Commons Attribution License, which permits use, distribution and reproduction in any medium, provided the original work is properly cited.

DOI: 10.1002/aisy.202400275

force is less than 2.5 N, which limits its applicability when connected to a robotic gripper that exerts a significant force. Other existing magnet-based textile sensors also prioritize high sensitivity and set the maximum measurable force low by designing the sensor to have a large number of Hall sensors placed in a thin structure.^[21–23] These examples demonstrate the trade-off of soft tactile sensors among sensor sensitivity, size, and durability. Their small size limits their force measurement range, while their large bulk makes them difficult to use in practical robotic grippers.

To address this issue, a soft tactile sensor must meet three criteria simultaneously:^[24,25] 1) compactness, 2) a wide measurement range, and 3) high localization accuracy and force resolution. Most tactile sensors used in robotic grippers are magnet-based.^[26–28] Although they have a simple structure and high sensitivity, their force measurement range tends to be limited. Our proposed sensor is an innovative magnet-based soft tactile sensor that satisfies three criteria.^[29] It uses magnetorheological elastomers (MREs) in a sandwich-like multilayer structure and incorporates a bottleneck DL model, as illustrated in Figure 1 and 4.

MREs are rubber-like solid materials made up of magnetically sensitive particles embedded in a nonmagnetic polymer matrix. They display a range of physical properties, including increased stiffness when exposed to an external magnetic field.^[30] MREs have gained significant attention in recent years due to their potential applications in various engineering fields.^[31–34] Due to the complex nature of MREs, studies that utilize them to create soft tactile sensors^[35] or attach them to grippers^[36] have regarded them simply as inductance markers or magnetic flux inductors. However, this approach has resulted in sensors with a limited force measurement range. Our proposed sensor uses a sandwich-like configuration to fully utilize the physical characteristics of the MREs and significantly expand the range of force measurement.

The multilayer structure of our sandwich-like configuration consists of layers of elastomers with distinct properties, resulting in higher stability of soft sensors.^[37–39] The proposed sensor has a sandwich-like structure with a top layer composed of an MRE, a middle flexible printable circuit board (FPCB) layer, and a bottom layer containing a rigid magnet. The top and bottom layers are more rigid than the middle layer. This design allows for high sensitivity and a wide force measurement range by increasing the degree of deformation of the middle sensing layer and tolerating a large external force.^[30,40] In addition, to enhance the functionality and accuracy of the tactile sensor, a bottleneck DL neural network that can effectively extract features from the data was utilized. This network addresses the interference caused by the mechanical hysteresis of the elastomer when an external force is applied to the sensor. It is used to measure the magnitude of the force, determine the point of contact, and classify the area of the object in contact. The classification of the area of a contacted object is a new capability that has not been identified in previous studies. This function enables the sensor to classify the area in contact with the object as either small or large, enabling the robotic gripper to identify the morphological configurations of asymmetrical or oddly shaped parts.

As a result, the proposed soft tactile sensor can measure a load of 3.63 kgf with 96.418% accuracy using a simple structure

comprising four Hall sensors and a thickness of 10 mm. Additionally, it can locate the source of the force with 96.857% accuracy when a 2 mm diameter object gradually applies an external force to the sensor. These characteristics exceed the payload capabilities of commercial soft grippers.^[41] In the following section, the design scheme of the proposed MRE-based soft tactile sensor is explained in detail. Section 2.1 describes each layer of the sandwich-like structure and explains the rationale behind the design of each layer. Section 2.2 provides a comparative analysis to determine the appropriate MRE for use in the soft sensor via COMSOL software. Section 2.3 covers the actual fabrication of the soft tactile sensor. Section 3 discusses the experimental setup and results of DL model training. Verification experiments and results for the sensors attached to a robotic gripper are presented in Section 4. The sensors accurately discriminated between the head and tail of a screw during the gripping process. Section 5 presents a summary of the results.

2. Sensor Design

2.1. Sandwich-like Multilayer Structure

While previous studies have utilized thin magnetic films to reduce sensor thickness,^[42,43] the objective of this study was to manufacture sensors for a robotic gripper capable of identifying industrial parts and withstanding a significant force in the single-digit kgf range. To achieve sufficient strength, this article proposes a new sensor design consisting of three layers—an MRE layer, an FPCB layer, and a magnetic layer—stacked in a sandwich-like configuration, as shown in Figure 1a.

The magnetic layer contains four hard cylindrical magnets (Neodymium, $\varnothing 3 \times 2$ T, 3100 G) embedded in a soft elastomer to enhance stiffness. The insertion of rigid bodies into the lower elastomer layer reduces the vulnerability of the FPCB layer to deformation by external forces, thereby protecting the FPCB from potential damage and abnormal operation. To enhance the measurement range of the soft tactile sensor, we incorporated four Hall sensors onto the FPCB layer, precisely aligned with the magnet's axis. This design reduces the negative effects of shear deformation on the electronics, which are typically caused by force on the soft tactile sensor. As a result, the structural stability improves the overall measurement range of the sensor system. In addition, the proposed structure deforms the MRE layer to bring it closer to the magnet layer. This allows the Hall sensor to measure the convergence of the magnetic flux vector to the point where the force is applied. It also effectively deforms the FPCB according to the shape and position of the indenters that generate the external force, thus providing meaningful sensor data, as shown in Figure 1b. However, conventional magnet-based soft tactile sensor designs typically consist of a magnetic field-generating layer and a sensing layer.^[44–46] When an external force is applied, only the magnetic field-generating layer deforms; this deformation is sensed by the sensing layer to measure the external force. The corresponding structure requires a small thickness between the two layers to benefit from measurement accuracy;^[22,23] however, a thin structure inevitably has a limited force measurement range.

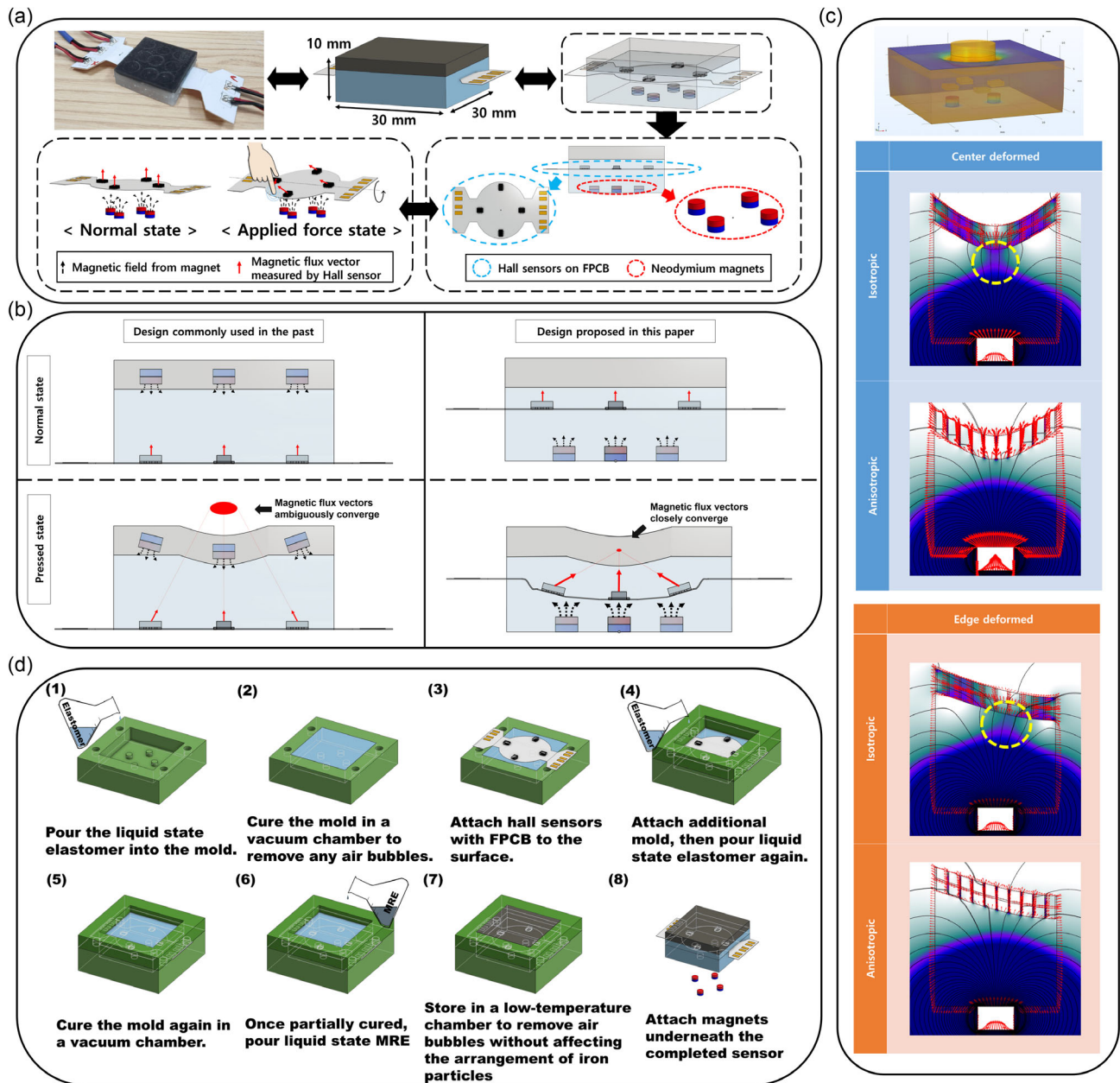


Figure 1. DL model-based soft tactile sensor system. a) Actual sensor geometry and schematic diagram of the sandwich-structured soft tactile sensors consisting of a bottom layer with magnets, a FPCB layer, and a MRE layer. When the external force is applied to the soft tactile sensor, three-dimensional (3D) Hall sensors can detect the deformations of the magnetic flux vectors. b) Comparative analysis of the structure proposed in this article (left) and a general soft tactile sensor structure (right). In the proposed structure, the magnetic flux data measured by the Hall sensor were more useful in identifying the contact location. c) Verification of performance change according to the internal structure of the MRE. COMSOL confirmed that the isotropic structure is more suitable for soft tactile sensors. d) The fabrication process of the proposed soft tactile sensor.

The proposed sensor has a thickness of 10 mm, which is suitable for measuring large forces while maintaining mechanical stability. Additionally, as can be seen in the verification experiment conducted in Session 4 of this article, this thickness is appropriate for situations where the attached robotic gripper picks up uneven objects and accurately recognizes the gripping shape of the object. Therefore, the soft tactile sensor has a

symmetrical thickness of 5 mm in relation to the FPCB at the center. According to ref. [47], the degree of deformation of the elastomer's pressurized and unpressurized zones varies depending on the ratio of the radius of the indenter r that exerts pressure on the sensor and the thickness D of the elastomer above the rigid structure. This can be divided into three cases: $r > D$, $r \approx D$, and $r < D$. For $r > D$, the strain energy density (SED) is

high in the region below the indenter. In contrast, for $r < D$, the SED is high in the exterior region. For $r \approx D$, the SED is similar in both regions. Here, SED represents the energy generated by internal stress and deformation, indicating the degree of object deformation. We used indenters with radii of 1 and 4 mm to train the DL model of the proposed sensor. The variance in elastomer deformation based on the indenter size can result in substantial differentiation between the gathered datasets, thereby aiding in the training of the DL model. Therefore, we set $D = 5$ mm to induce the case of $r < D$, where deformation is larger in the indented area than in the unindented area, and the case of $r \approx D$, where the deformation of both areas is similar.

2.2. MRE

After determining the efficient structure of a sensor, we designed MREs suitable for the structure. The unique mechanical and magnetic properties of MREs, which exhibit stiffness enhancement and field concentration (FC) properties, enable further improvements in sensor performance that previous soft sensors could not achieve. In studies such as,^[30,40,48,49] the combination of an MRE layer and a conventional elastomer layer has been shown to offer improved stability, including extended lifetime and high fatigue resistance. This combination can also serve as a sensor because of the contrasting mechanical properties of the two layers. However, if the physical properties of the layers of the sandwich-like structure differ significantly, the layers may separate when a large external force is applied. We have found that the iron particle content should be 15 wt% in order for the MRE layers to have adequate stiffness.^[50,51] Furthermore, to prevent damage to the MRE layer from constant exposure to external forces, we increased the thickness of that layer to 2 mm, which is greater than the typical MRE (=1 mm).^[52–59] This adjustment enhanced the storage modulus, indicating the elastomer's capacity to store energy.^[60]

The FC function of the MRE also enhances the sensitivity of soft-textile sensors by increasing the magnetic flux strength that Hall sensors can detect.^[61] This function introduces a unique distinctive capability known as contact area classification.^[62] The isotropic and anisotropic arrangement of MRE particles affects the extent of their FC effect.^[63,64] We used COMSOL to determine which of the two structures was more effective in a sandwich-like configuration (Figure 1c). In the simulation, the soft textile sensor had a sandwich-like structure containing a 2 mm thick MRE layer. Specifically, the MRE layer consisted of elastomer and uniformly distributed iron particles ranging from tens to hundreds of microns in size (particle size has minimal effect on the magnitude of the FC function).^[65] The COMSOL results showed that the isotropic structure increased the magnetic flux intensity by 7.32% compared with the anisotropic structure. The magnetic flux converged to the point of external force generation, confirming the performance of the proposed sensor design. The soft tactile sensor designed with this structure has three stages: 1) a data generation process, 2) a DL model training process, and 3) verification experiments in which the sensor is attached to a robotic gripper, as shown in Figure 4 and 7.

2.3. Sensor Fabrication

Figure 1d illustrates the manufacturing process of the sensor. First, the elastomer (Xinus Silicone SH2115) is poured into the lower mold and allowed to partially cure. The mold, which has four small pillars for the neodymium magnets, was fabricated using a 3D printer. Place the FPCB with the four Hall sensors on top of the 80% cured elastomer. Ensure the four Hall sensors are aligned with the small pillars of the lower mold on the same z-axis. Next, assemble the upper mold and fill it with elastomer to cover the FPCB. When the upper elastomer layer is $\approx 80\%$ cured, pour a layer of 15 wt% iron MRE on top and allow it to cure completely. After curing, the fully assembled tactile sensor is removed from the mold, and a magnet is placed underneath. The dimensions of the finished sensor are 30 mm \times 30 mm \times 10 mm.

3. DL-Based Sensor Training

3.1. Experimental Setup

The simple bottlenecked DL model was utilized as an algorithm for the sensor in this study. The UR3 robot (Universal Robots) was used to acquire rich and precise data for model training. The experimental setup involved attaching a load cell (CDFS-100 kg, BONGSHIN) and an indenter to the tool flange of the UR3 robot. Subsequently, a randomly selected area of the soft tactile sensor was pressed. During the experiment, the vector values provided by the four Hall sensors were recorded, along with the force value measured by the load cell and the incidence position value. The precision of the UR3 robot was 0.1 mm, while the precision of the load cell was 0.01 kgf.

Two types of indenters were used in the study to evaluate the soft tactile sensor, as shown in Figure 2a. The first indenter was an 8 mm diameter cylinder, which resembled the large area of an asymmetric industrial part, such as the head of a screw. To ensure efficient data labeling and training of the artificial neural network model, the sensor surface was divided into nine sections of approximately the same size as the indenter surface, as illustrated in Figure 2b.

Even when the pressure resulted in unfavorable deformation, subdividing the sensor area helped the model accurately identify the location of the applied pressure. The second indenter was conical in shape with a hemispherical tip measuring 2 mm in diameter, simulating a sharp object. The 30 mm-wide sensor area was divided into smaller 2.5 mm-wide subareas. The 2.5 mm spacing was chosen to allow the DL model used for the proposed sensor to exhibit contacted object area classification functionality. For the model to learn effectively, the magnetic flux data collected during the indenter-mediated application of external force to the soft tactile sensor should exhibit a significant difference; the classification model should capture this disparity. However, if the spaces between external force zones are smaller than the diameter of the indenter (i.e., 2 mm), the classification accuracy will decrease. Therefore, we divided the external force zones with a spacing of 2.5 mm, which is larger than the diameter of the indenter. During the pressing process, the outermost sensor section was excluded from the experiment because the

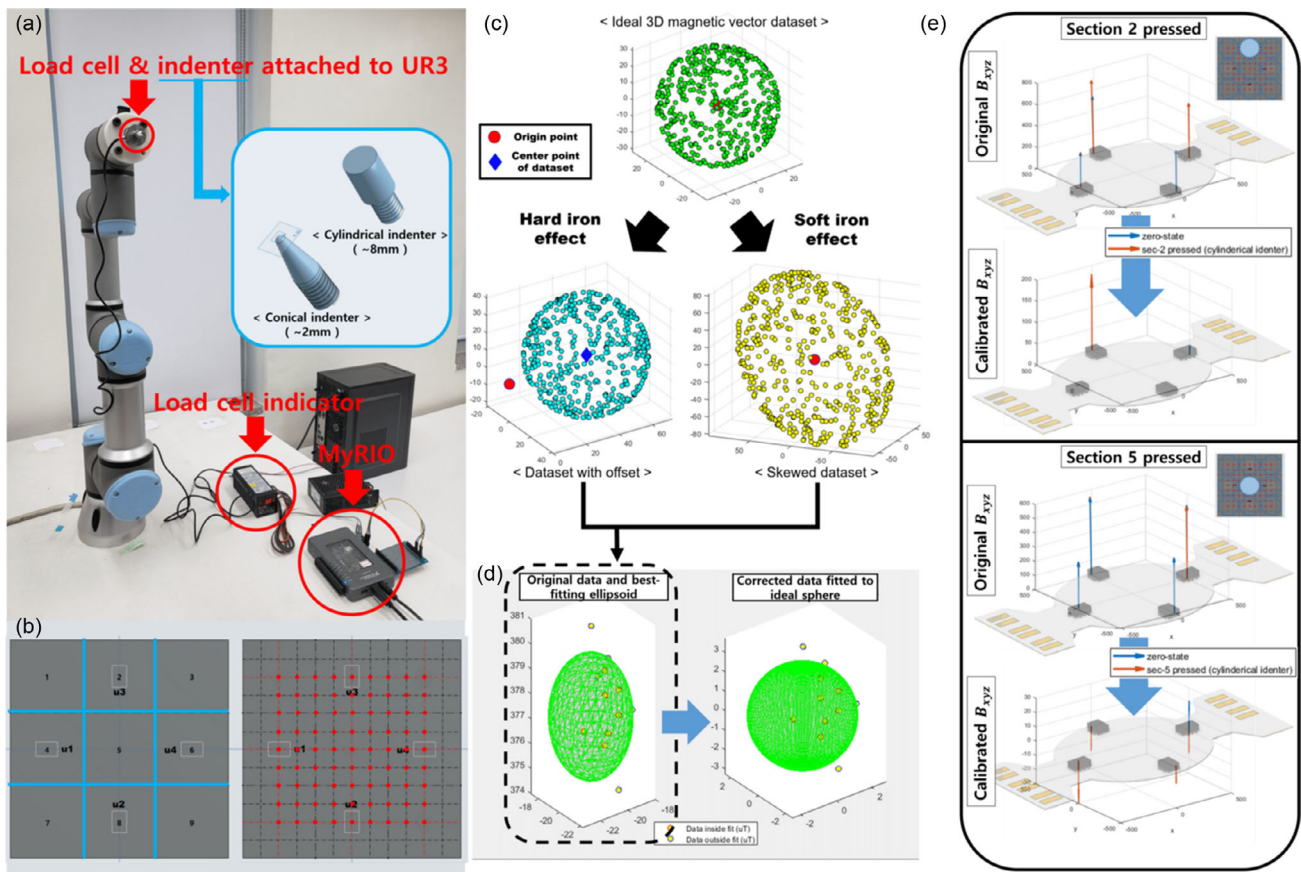


Figure 2. Experimental setup and calibration of soft-iron/hard-iron effects. a) A load cell and indenter are attached to UR3. The load cell measures external force transmitted to the laptop through MyRio. Indenters are used to compress the soft tactile sensor, with cylindrical and conical indenters mimicking the head and tail of a screw, respectively. b) Top-down view of the soft tactile sensor's MRE layer. The area of the soft tactile sensor is divided to determine the location of external force generation. When using a cylindrical indenter, the sensor is divided into nine sections (left); when using a conical indenter, the sensor is divided into 81 sections (right). c) Soft-iron/hard-iron effect. Ideal data values are offset (hard-iron effect) and skewed in a specific direction (soft-iron effect) by their surroundings. d) Visualization of original data from the Hall sensors (left) and calibrated data (right). e) Calibration performed on actual data collected while pressing section 2 (upper) and section 5 (lower). Calibrated vector data have a uniqueness that allows discrimination of individual points.

indenter was prone to slipping out of the peripheral region. Accordingly, 81 points were selected for the research experiment.

3.2. Sensor Calibration

The 3D Hall sensors on the FPCB have been calibrated to ensure accurate magnetic field measurements. This process is essential as it is affected by various factors, such as the arrangement of the particles inside the MRE and the presence of an external magnetic field. The primary goal of the calibration was to remove the soft iron and hard iron effects from the Hall sensor, as illustrated in Figure 2c.^[66,67] The soft iron effect is observed when a nearby ferromagnetic object, such as an MRE, deflects or distorts the magnetic field, changing its direction. In contrast, the hard iron effect occurs when the magnetic field generator is near the sensor. The soft iron and hard iron effects can cause a slight offset in the Hall sensor's measurements. To correct for these effects, we applied adjustments for stretching, tilting, and

shifting of the measured flux data, as illustrated in Figure 2d. During the calibration process, the magnetic force data from the four Hall sensors were recorded in a zero state, indicating that no external force was applied. The recorded magnetic data values were used to create a 3D ellipsoid to fit the data.

The center point of the 3D ellipsoid was then relocated to the origin, and a correction filter was created to transform the ellipsoid into a sphere to address hard and soft iron effects. The correction process was performed individually for each of the four Hall sensors to ensure that all sensors produced normalized triaxial magnetic field vectors. The normalized vectors were visualized, as shown in Figure 2e. The top portion of Figure 2e shows the cylindrical indenter applying no force to Section 2 of the soft textile sensor and then applying a force of 1.2 kgf (blue and orange arrows, respectively). The bottom portion of the figure depicts the same scenario repeated for Section 5 of the soft sensor. For additional visualizations of the sensor data, please refer to Figure S2 and S3, Supporting Information.

3.3. Data Generation

To investigate the compression characteristics of the soft tactile sensor, two experiments were conducted using 9-section and 81-section models, as illustrated in Figure 2b. Each experiment consisted of a zero-state measurement process and a pressing process during which real-time recordings were made of the magnetic flux vector information, the classification number of the pressed section, and the magnitude of the pressing force. In the zero-state measurement process, 500 data sets were collected from each of the four Hall sensors to create a calibration filter while the tactile sensor was in a zero-state. This measurement process was performed prior to the pressing process and during every third cycle of the pressing process due to possible changes in the elastomer layer and MRE layer properties associated with continuous deformation. During the pressing process, a randomly selected section of the soft tactile sensor was compressed by an indenter to a depth of 7.62 mm, with a maximum recorded force of 3.73 kgf. Considering the nonlinear mechanical properties of the elastomer,^[68–74] the pressing process was repeated 17 times within 5 min at a constant speed of $\approx 0.86 \text{ mm s}^{-1}$. This is because the physical properties of the elastomer vary depending on the degree of prestressing, the distance between the previously compressed area and the newly compressed area, and the pressing speed.^[75–77] This phenomenon is

more severe in the MRE layer due to the pressing-related destruction and subsequent reformation of the internal particle structures during the rest periods.^[78] $\approx 35\,000$ data points were obtained in the 9-section case and 67 000 data points in the 81-section case, both with a 20-Hz sampling rate. These data points were then calibrated using the filter created by the zero-state measurement process. An artificial neural network trained with these data points is expected to have high accuracy in various situations.

3.4. Data Validity and Sensor Reliability

Before commencing data training, we validated the collected data and checked the reliability of the sensors. We first performed a t-distributed stochastic neighbor embedding (t-SNE) visualization to ensure that the data collected over multiple rounds showed correlation and consistency. T-SNE is a nonlinear dimensionality reduction technique that computes and optimizes the similarity between high-dimensional and low-dimensional data using a probability distribution. Figure 3a visualizes the similarity between high-dimensional data as the proximity between low-dimensional data. Data with the same section labels are marked with the same color. It can be observed that both 9-section and 81-section data are generally clustered with data of the same color, indicating a high similarity between them. Surprisingly, it is observed that the data is clustered in a

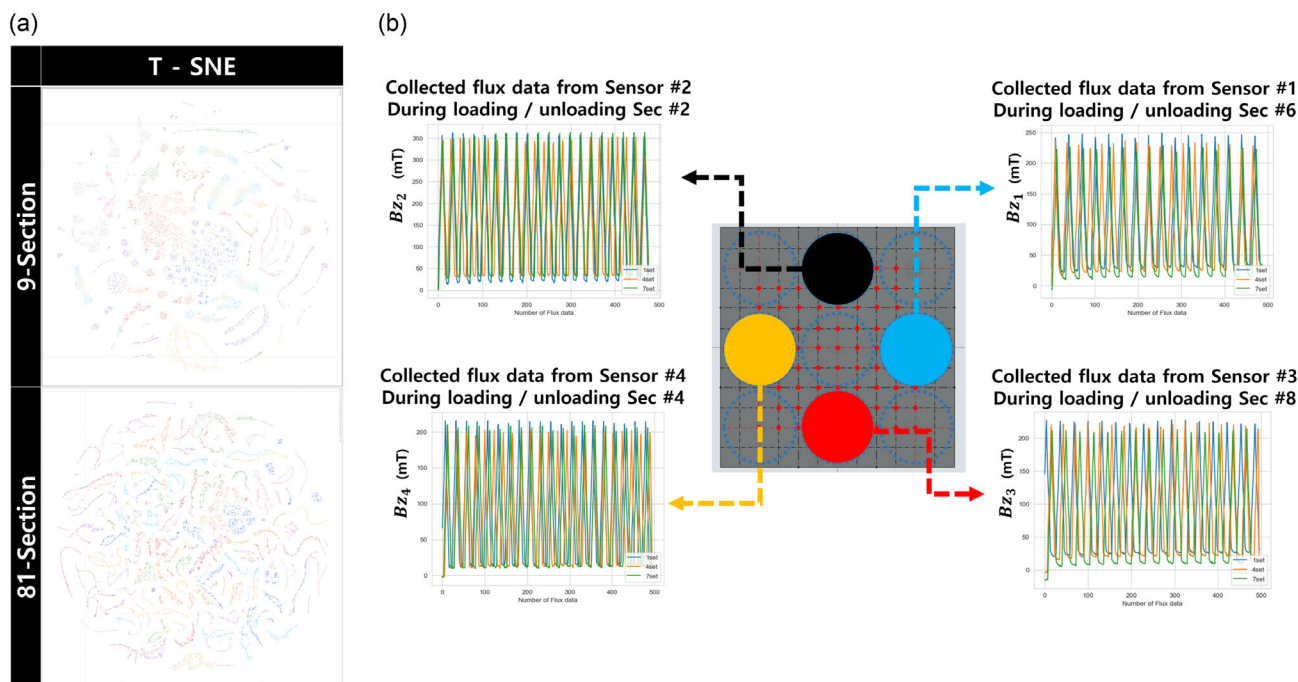


Figure 3. a) The t-SNE visualization displays a “9-section dataset” collected using an 8 mm-diameter cylinder indenter on the left and an “81-section dataset” collected using a 2 mm-diameter cone-shaped indenter on the right. The data are well separated from each other. Additionally, due to the elastomer’s hysteresis, the data clusters into a specific curve shape. b) This image visualizes the calibrated sensor data measured when an external force is applied to the sensor, proving the reliability of the sensor. To observe the dynamic changes in the sensor data, an external force was applied with an 8 mm cylinder indenter to sec 2, 4, 6, and 8 where the Hall sensor is located. Three sets of data were measured for each zone: (1 set) measured when the external force was first applied to the zone, (4 set) measured after 500 deformations, and (7 set) measured after 1000 deformations. The data visualized is based on the B_z data, which shows the largest rate of change, and the depth at which the indenter pressed the sensor is 7.62 mm in all four sections. The larger the previous deformation of the sensor, the smaller the maximum value of the measured data, but the overall pattern is the same, showing that the proposed sensor is stable over 1000 deformations.

thread-like pattern. This is probably due to the hysteresis caused by the sensor's constant exposure to external forces.

Figure 3b compares the data output from 1000 consecutive pokes with an 8 mm cylinder in the four zones where the Hall sensor is located inside the soft sensor. The colors blue, orange, and green represent the Hall sensor data at the first poke, after 500 pokes, and after 1000 pokes, respectively. This illustrates how the intensity of the Hall sensor data changes depending on the amount of external force the soft sensor has experienced. The strength of the signal measured by the Hall sensor decreases slightly as it experiences more deformation, but the overall pattern of the sensor signal remains consistent. Specifically, there is a significant difference between the sensor data before exposure to external forces and the sensor data after exposure to external forces, but the latter is very similar. By confirming that the data pattern remains consistent even after 1000 deformations, we can verify that the proposed sensor is durable enough to generate a consistent data pattern even after 1000 consecutive deformations.

3.5. Artificial Network with Hysteresis Compensation

Previous studies have utilized DL neural networks with nonlinear activation functions to process nonlinear data from elastomer-based soft tactile sensors.^[29,79–82] Hysteresis is a nonlinear property exhibited by elastomers, including MREs, that results in differences in mechanical behavior during loading and unloading.^[83–85] Figure 4c demonstrates the phenomenon, showing experimental data collected by a load cell. The magnitude of the measured force varies due to the elastomer's hysteresis, despite the data being collected at the same node speed (0.86 mm s^{-1}) and compression depth of the soft tactile sensor. Furthermore, the study indicates that the maximum measured force decreases as the number of compressions increases. Two DL neural networks were utilized in this study: MLPClassifier and MLPRegressor (MLP, multilayer perceptron), both available in the widely used Python machine learning library, scikit-learn. The MLPClassifier is utilized in classification learning to make predictions regarding one of several predefined class labels.^[86] The sensor uses a label for location instead of an XY coordinate system; therefore, a localization model was employed for this neural network. The MLPRegressor is utilized as a model for measuring force magnitude in regression training and predicting continuous data.^[87] This model analyzes the correlation between load cell data and Hall sensor data that change during repeated loading and unloading of the soft sensor.

The MLPs used in this article consist of four layers, as illustrated in Figure 4b. The third layer is a bottleneck structure, where the layer size is significantly reduced compared to the front and back layers, effectively extracting features from data.^[88] The MLPClassifier model generates a position value for the external force when the magnetic flux data from the four Hall sensors (12 input data points) are inputted. The MLPRegressor utilizes the result as an input along with magnetic flux data (consisting of 13 input data points) to determine the magnitude of the external force. In terms of layer size, slight variations in optimization were observed depending on the type of data used during training. In general, the size of the bottleneck layer was 30 or 40, while

different sizes from 230 to 300 were used for the remaining layers.

Two experiments were conducted to confirm the effectiveness of tagging the loading and unloading states of data: separation learning and summation learning. In the first experiment, separation learning, the 9-section and 81-section datasets were divided into three cases: data measured during loading, data measured during unloading, and data randomly mixed from the previous two cases. Six DL models were generated using only these data, and their performances were evaluated to assess the importance of state tagging. After confirming its importance, in the second experiment, summation learning was applied, combining the 9-section and 81-section data sets to train a DL model for determining whether the measured magnetic flux data were caused by a cylindrical or conical indenter.

3.5.1. Separation Learning

To investigate the tagging of loading and unloading states by considering elastomer hysteresis, a separation learning experiment was performed. First, the dataset collected from the four 3D Hall sensors, measuring the magnetic flux during pressing on the 9-section and 81-section elastomer datasets, was divided into three states: loaded, unloaded, and nondivided. An MLPClassifier model was then trained on each dataset to estimate the location of the external force on the sensor. In the next step, the MLPRegressor model was used to estimate the force magnitude by incorporating the actual external force location data into the same dataset. The accuracy of both models in predicting the location and magnitude of the external force was evaluated.

Table 1 displays the results of evaluating the accuracy of models that predict the location and magnitude of external forces. Here, the models were trained with a dataset that either included or excluded hysteresis information. The location estimation models, generated by MLPClassifier, exhibited similar prediction accuracies. The model achieved accuracies of 99.644% and 96.747% in 9-section case and 81-section case, respectively, when trained without hysteresis information, which is comparable to the accuracy achieved when trained with hysteresis information. However, the force estimation models generated by MLPRegressor exhibited differences in performance. When the model was trained on a dataset without hysteresis information, the force measurement model's accuracy and mean square error (MSE) were 89.699% and 0.0483 kgf^2 for the 9-section case, and 94.971% and 0.0322 kgf^2 for the 81-section case, respectively. Improvements in force calculation accuracy were observed for force models trained on datasets containing hysteresis data. The accuracy of force calculation for the loading and unloading states of 9-section was improved by 4.22% and 5.372%, respectively. The corresponding MSE values decreased by 0.0152 and 0.0238 kgf^2 . In 81-section, the accuracy of force calculation improved by 1.447% and 1.537%, respectively; the corresponding MSE values decreased by 0.0063 and 0.0077 kgf^2 . The accuracy of the MLPRegressor model was measured using the prediction coefficient of determination.

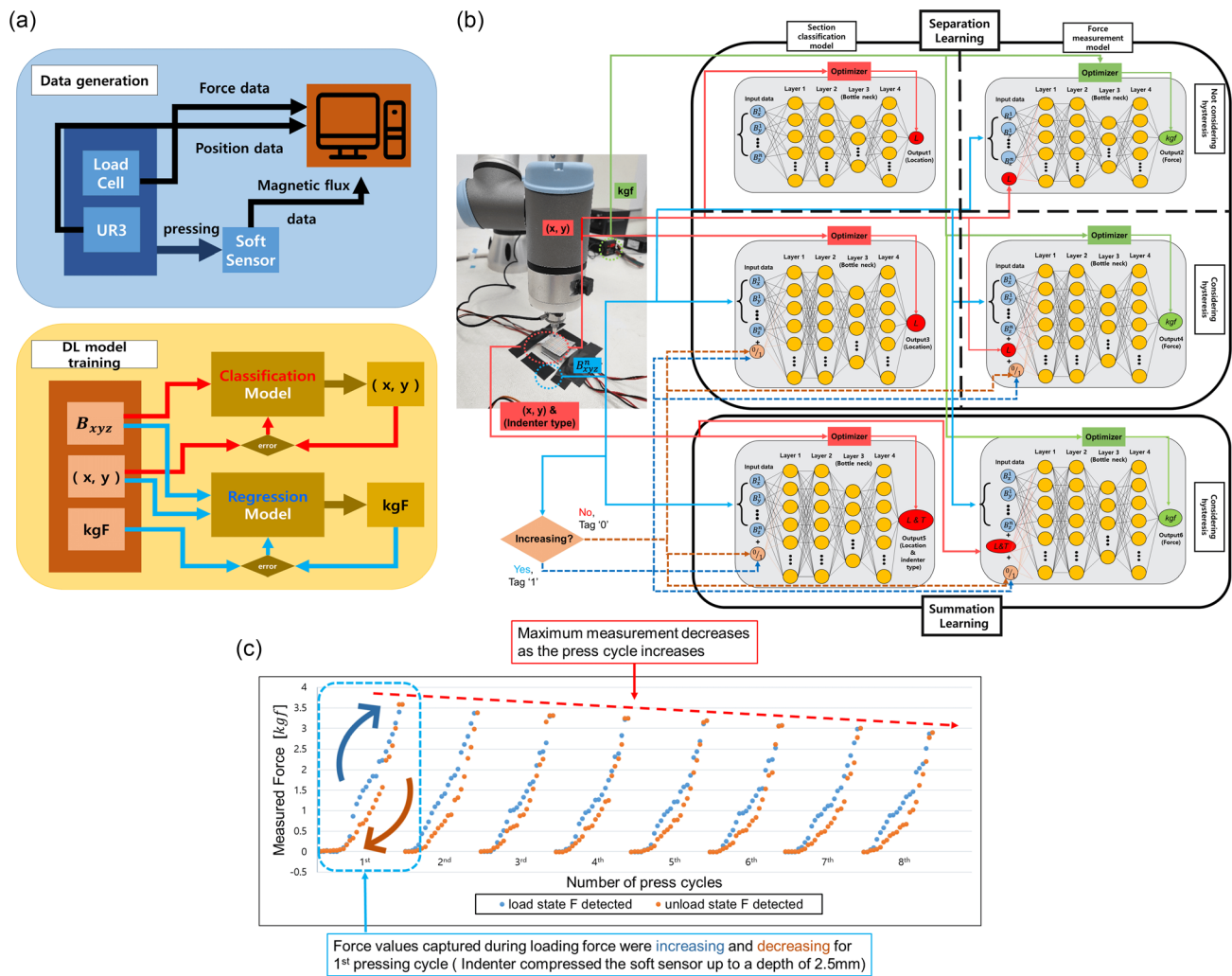


Figure 4. a) Flowcharts showing data generation and the model learning process. Magnetic flux data are represented as B . Figures with blue and yellow backgrounds briefly are summarized Sections 3.3 and 3.4. b) The training process of four-layer MLP. The third layer has a bottleneck structure with a size of 30–40, and the sizes of the remaining layers are ≈ 230 –300. Rectified linear unit was used as the activation function, and the learning rate was 0.0001–0.00005. When learning the hysteresis model, we tag whether the soft tactile sensor is in the loading or unloading state by identifying the change in flux vector size. Among the four models introduced, the top two are models that do not consider elastomer hysteresis, whereas the bottom two are models that consider elastomer hysteresis. c) Force data obtained by compressing the soft tactile sensor five times with the UR3 robot. Two phenomena were observed: hysteresis by loading/unloading and a change in physical properties as the prestress state continues (maximum measurable force decreasing).

3.5.2. Summation Learning

The objective of the summation learning experiment was to enhance the capabilities of our soft tactile sensor by merging data from the 9-section and 81-section datasets. We hypothesized that a DL neural network trained on this merged dataset would accurately classify the surface shape of the indenter. The experiment involved modifying the structures of the DL models, as depicted in the lower part of Figure 4b. The MLPClassifier was modified to predict the expected location value and the type of node contacted. Similarly, the MLPRegressor was adjusted to accept input data with node-type information.

The results are presented in the lower part of Table 1, with force estimation accuracy and MSE of 96.357% and

0.02447 kgf^2 for loading, and 95.642% and 0.02801 kgf^2 for unloading, respectively. The sensor exhibited an accuracy of 91.761% in discriminating between different areas. The area discrimination accuracy was determined by calculating the proportion of cases in which the model predicted the correct answer for both the shape and contact area values of a node. The study showed that the summation model accurately performed area discrimination and node classification with over 90% accuracy while maintaining a similar level of force prediction accuracy compared to the separate learning model. In conclusion, the summation learning model enabled the soft sensor to determine the magnitude and location of the external force and classify the contact type (point or surface). This sensor has a wide range of potential applications, including gripping objects of various sizes with robotic grippers.

Table 1. Performances of the location determination and force measurement (force calculation) models. For determining localization performance, the 9-section model and 81-section model are evaluated based on the accuracy of area discrimination, while the summation model is evaluated based on its accuracy to simultaneously match the node type and contacted area.

Parameters [DL model]	Area discrimination accuracy [%]	Force calculation accuracy [%]	Force calculation MSE [kgf ²]
9-section loaded	99.712 ± 0.271	93.919 ± 0.641	0.0331 ± 0.0017
9-section unloaded	99.504 ± 0.304	95.071 ± 1.072	0.0245 ± 0.0018
9-section nondivided	99.644 ± 0.343	89.699 ± 0.501	0.0483 ± 0.0037
81-section loaded	96.857 ± 0.116	96.418 ± 0.976	0.0259 ± 0.0044
81-section unloaded	96.496 ± 0.082	96.508 ± 0.725	0.0245 ± 0.0029
81-section nondivided	96.747 ± 0.094	94.971 ± 0.775	0.0322 ± 0.0014
–	Area discrimination and contact	–	–
–	Node classification accuracy [%]	–	–
Summation model loaded	91.759 ± 0.194	96.357 ± 0.815	0.0244 ± 0.0007
Summation model unloaded	91.763 ± 0.211	95.642 ± 0.725	0.0280 ± 0.0012

3.5.3. Model Performance Check

To validate the performance of the trained models, we evaluated the classification model using a confusion matrix and the regression model by comparing actual and predicted force. **Figure 5** displays the performance of the three location classification models, including two models trained after partitioning the collected dataset based on load/unload state and one nondivided model. In the case of 9-section, the models frequently misjudged the zero state when there was no external force and when force was applied to Section 1. This was confirmed when a weak force was applied to Section 1 and changes in the Hall sensor data did not appear immediately. In the 81-section case, the model that learned the unloaded state data often confused it with Section 3 directly above when Section 12 was pressed and with Section 4 when Section 13 was pressed. The root cause of these errors was identified as being due to the geometry of the FPCB, which is horizontally elongated. It was determined that these errors could be resolved by modifying the design of the FPCB. This conclusion is supported by the findings presented in Figure S4 and S5, Supporting Information. In the summation model case, an even distribution of accuracy was observed across all areas.

Figure 6 illustrates a comparison between the actual force measured by the load cell and the force predicted by the regression models when the soft sensor was pressed to a depth of up to 7.62 mm. The analysis was conducted for up to 16 presses due to the physical properties of the elastomer, which were confirmed in Section 3.4 of the paper. The model's predicted values were anomalous for up to the 16th press due to the large change in physical properties when the elastomer first undergoes deformation. Afterward, they were omitted because they showed similar behavior. The top of the figure shows the situation with an 8 mm cylindrical indenter and the bottom shows the situation with a 2 mm conical indenter. In general, models that learned only one indenter data showed better prediction values than summation models that learned all of the indenter data in both situations. However, the 81-section models, illustrated at the bottom of the figure, exhibit fluctuations in the prediction values,

unlike the 9-section models, which show stable force predictions. This phenomenon occurs primarily in regions where the magnitude of the external force is less than 1 kgf. It appears that this is due to the inability of four Hall sensors alone to precisely track small deformations in a small area. This directly leads to errors in the position prediction value used as input to the force prediction model. In addition, both the 9-section and 81-section situations show a significant discrepancy between the actual and predicted values during the initial piercing of the sensor. However, in subsequent cases, the predicted value closely follows the actual value. This phenomenon is attributed to the difference in hysteresis between the undeformed and deformed elastomer, as shown in Figure 3b. Additional indicators that can demonstrate the performance of the regression model, such as the Kernel Density Estimation Plot, the Scatter Plot, and the Violin Plot, are presented in Figure S6–S8, Supporting Information.

To determine the suitability of MLP as a DL model for the produced sensor, a performance comparison was conducted with MobileNet-V2 and MobileNet-V3. MobileNet is a widely used neural network that can be employed in limited environments, such as mobile devices, by significantly reducing model size and computational complexity through inverted residuals and bottleneck structures. As the MobileNet model uses the same bottleneck structure as the MLP model presented, we deemed it appropriate as a comparison group. We made several modifications to enable MobileNet to learn 1D array data and train location estimation accordingly. We then compared its performance by training it on the 9-section dataset, 81-section dataset, and Summation dataset of the unloaded state. After conducting a study on separation learning, it was found that the MLP model outperformed MobileNets. Specifically, the MLP model showed 7.1% and 8.4% higher accuracy on the 9-section dataset and 2.2% and 3.9% higher accuracy on the 81-section dataset, respectively, when compared to the MobileNet-V2 and V3 models. However, on the Summation dataset, the MLP model had an accuracy of 1.9% higher than MobileNet-V3, but 0.6% lower than V2. The Supplementary Materials display Figure S9 and Table S1, Supporting Information, which present detailed learning outcomes. In conclusion, we confirmed that the MLP structure

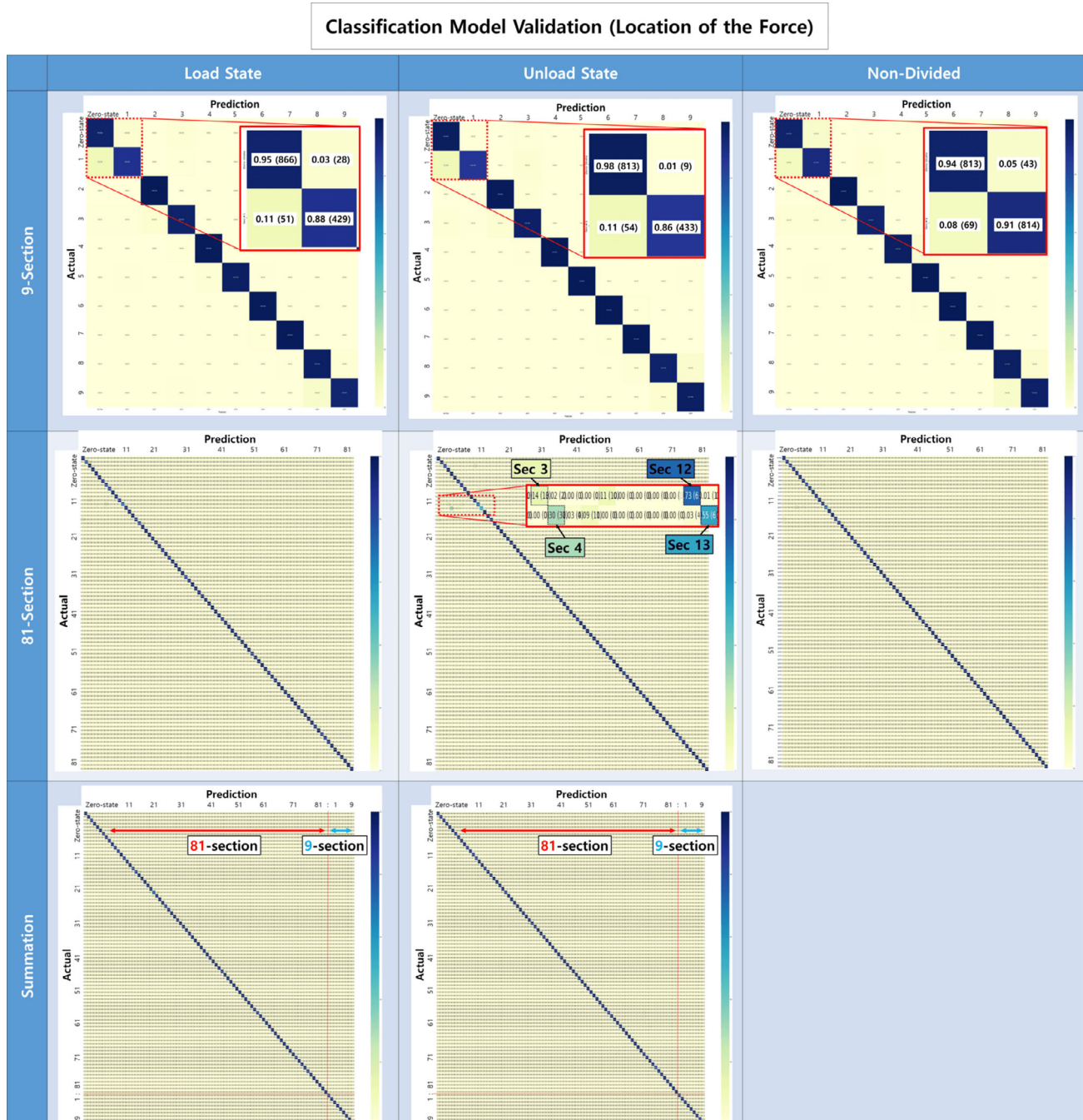


Figure 5. Visualization of the performance of the classification model to determine the location of the external force through the confusion matrix.

exhibited superior overall performance and deemed it appropriate for the proposed sensor.

4. Adoption in a Robotic Gripper

4.1. Experimental Setting

The proposed tactile sensor can measure force magnitude and position while classifying the force as point contact or surface

contact. In particular, the ability to classify the force as point contact or surface contact is a unique feature not available in previous sensors. An additional experiment was conducted to demonstrate the potential applications of this feature, as shown in Figure 7a.

To evaluate the performance of the developed sensors when attached to a real robotic gripper, two sensors were attached to the gripper of an OpenMANIPULATOR-X (ROBOTIS) to pick up screws, as shown in Figure 7b. The screw was selected due to

Regression Model Validation (Magnitude of the Force)

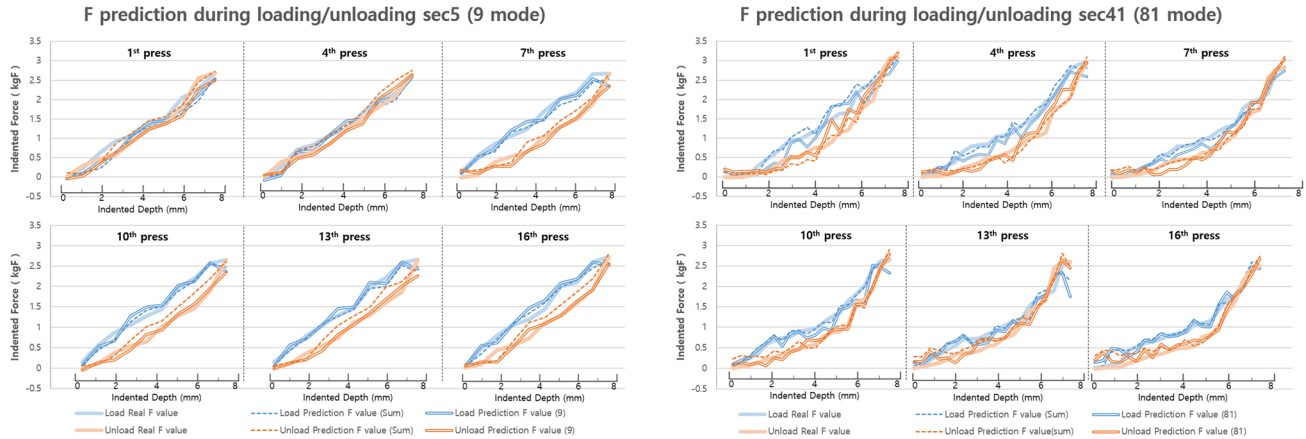


Figure 6. Comparing the predicted values of the trained force measurement models with the ground truth values obtained from the measured data when an external force is applied to the center of the proposed sensor. The figure on the left compares the force values predicted by the “9-section” models and the “Summation” models with the actual F value measured by the load cell when the center of the sensor is pressed by a cylinder indenter. In the case of the “9-section” models, the “9-section loaded” and “Summation loaded” models were employed when the cylinder indenter was in the process of loading, while the “9-section unloaded” and “Summation unloaded” models were applied when it was unloading. The figure on the right depicts the same environment using a cone-shape indenter to press the sensor with “81-section” models instead of “9-section” models.

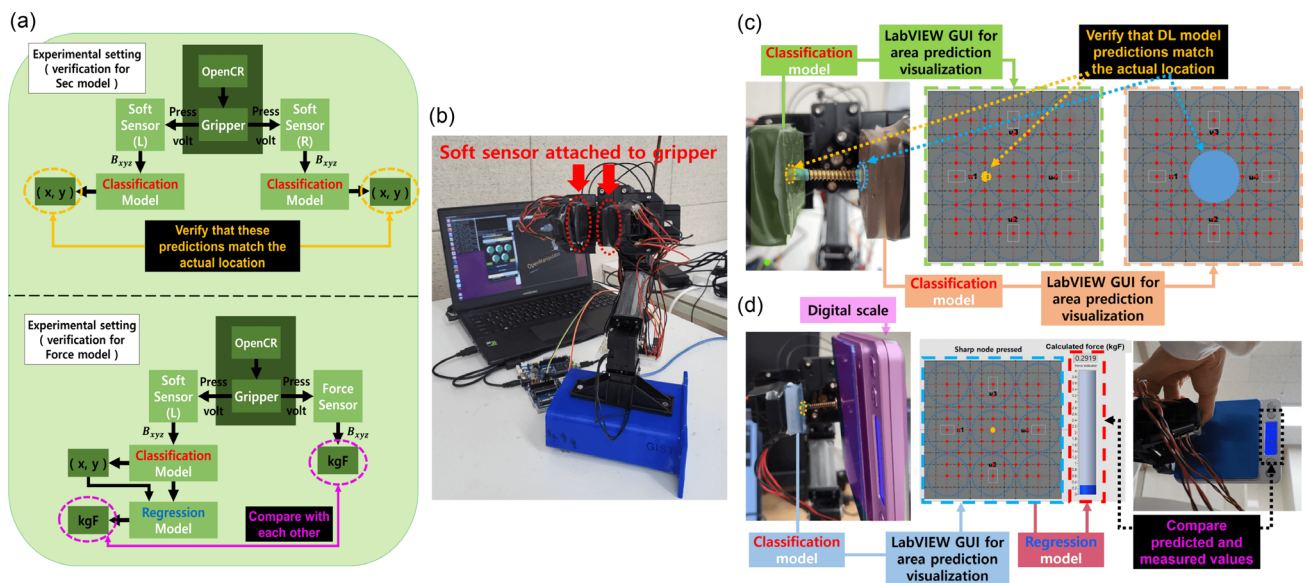


Figure 7. a) Flowcharts showing and sensor performance verification process. b) A view of the soft tactile sensor attached to the gripper of the OpenMANIPULATOR-X for functional verification experiments. c) Experiment for verification of section-classifying function. When the gripper grips the screw horizontally, the sensor on the left and the sensor on the right recognize the tail and head of the screw. Recognition of point contact is indicated by orange circles, and recognition of face contact is indicated by blue circles. d) Experiment for verification of the force-sensing function. The force value was measured by the soft tactile sensor (attached on the left) and the digital scale (attached on the right) while the gripper gripped the screw. The force value predicted by the force calculation model showed 91% accuracy compared with the force value measured by the digital scale.

its head and tail, which are similar to the cylindrical and conical indenters utilized for DL neural network training. Identifying the positions of these ends allows the screw configuration to be tracked. The summation DL neural network for the two sensors was trained prior to testing. The gripper held the head and tail of the screw at a relatively high speed (20 mm s^{-1}), and

all magnetic flux data generated during this process were collected. The data were then postprocessed into a summation DL model. The resulting GUI is shown in Figure 7c,d. The purpose of the experiment was to demonstrate the novel ability of the sensor to classify force as point contact or surface contact.

Table 2. Comparison of the proposed and previously developed sensors.

		Localization acc.	Force acc.	Force range	Sensor size [mm]
Capacitance based	K. Kim ^[10]	–	–	1.6 N	5 × 5 × 2.2
	T. Yao ^[90]	–	≈1.62% error	0.7 N	20 × 11.5
	Y. Zhang ^[89]	–	0.02 N	3 N	8 × 2
Optic based	R. Li ^[7,9]	0.14 ± 0.055 mm	RMSE = 0.668–1.856 N	1.4 N	13 × 17 × 30
	V. KaKani ^[91]	0.109–0.1396 mm	0.022 N	1 N	44 × 72
Hall sensor based	Y. Yan ^[43]	0.1–0.06 mm	RMSE = 0.15–0.01 N	2 ≈ 8 N	20 × 20 × 5.6
	R. Bhirangi ^[20]	99.58 ± 0.34%–87.00 ± 11.81%	MSE = 0.005 ± 0.002 N ² – 0.142 ± 0.025 N ²	2.5 N	20 × 20 × 3
	Ours	99.62 ± 0.34%–91.76 ± 0.20%	MSE = 0.0331 ± 0.004 kgf ² –0.0244 ± 0.001 kgf ²	3.73 kgf	30 × 30 × 10

4.2. Experimental Results

In Figure 7c, the blue circle at the center of the sensor indicates surface contact, while the slightly skewed orange circle represents point contact. This approach allows the conclusion that the screw is placed near the center of the gripper in a slightly twisted shape, which is consistent with the actual screw configuration. Therefore, when the sensor is used to grip a nonuniform object, the user can obtain information about the object's position in the gripper and the magnitude of the gripping force, as well as the current object configuration. The effectiveness of the soft tactile sensor's ability to measure force when integrated with the gripper was confirmed in an additional experiment. The experimental setup involved attaching the soft tactile sensor to one side of the gripper while attaching a force sensor to the other side; a screw was gripped in this configuration, as shown in Figure 7d. The measurements obtained from the soft tactile sensor and the summation model were compared with the measurements obtained from the force sensor (I2000 digital scale, minimum unit of measurement: 0.01 g). The resulting force accuracy of the DL summation model in the validation experiment (91.9%) was lower than the accuracy validated in Table 1. The observed discrepancy is attributed to the variation in the indenter material used during the experiment. The DL model was trained using nonconductive plastic indenters, while the validation experiments utilized metal screws that affect the magnetic flux. However, the area discrimination function estimated the exact location. These results successfully demonstrated the advantages of the MRE sensor over previously developed sensors. Unlike thin sensors with limited force measurement capabilities, our MRE sensor design has a wide measurement range and is able to more accurately determine object posture in practical applications. Further details on the experimental setup and results can be found in Figure S10, Supporting Information.

5. Conclusion

Table 2 compares the performance of the proposed sensor with various soft sensors. The new sensor is designed to maintain high measurement accuracy while withstanding high payloads in real-world environments. When comparing the maximum measurable force with the thickness of the sensor, the proposed

sensor recorded 3.67 N mm^{−1}, while refs. [20,89] recorded 1.5 and 1.43 N mm^{−1}, respectively, and the rest of the sensors performed below 0.83 N mm^{−1}. Notably, ref. [90], which has a similar thickness to the proposed sensor, showed a performance of 0.06 N mm^{−1}, confirming that this new sensor has a high force measurement range (≈3.73 kgf) relative to its thickness. The proposed sensor uses hysteresis analysis and DL to achieve high spatial resolution (2.5 mm, with over 96% accuracy), reliability for over 1000 deformations, and a unique touch area classification capability that can compete with other soft sensors. However, the design of the sensor to measure large forces reduces its temporal resolution. The circuit was designed with a low temporal resolution of 20 Hz to ensure more stable data values. Future modifications will improve the temporal resolution by introducing more effective data filtering. The proposed sensor has a dynamic range of 1:370, which is an acceptable level of accuracy for a robot picking up a bolt or nut. Future work will focus on developing the sensor for multiple contact and shear force sensing, miniaturization, and higher accuracy. The utilization of advanced MRE sensors in robotic manipulators will enable stable adjustment of the gripping posture, allowing for more precise movement of objects without the need for additional sensors or equipment.

Supporting Information

Supporting Information is available from the Wiley Online Library or from the author.

Acknowledgements

This work was supported in part by the GIST Research Project (RS-2023-00303777) and the GIST Research Institute (GRI) GIST-Korea Culture Technology Institute research Collaboration grant funded by the GIST in 2023.

Conflict of Interest

The authors declare no conflict of interest.

Data Availability Statement

The data that support the findings of this study are available from the corresponding author upon reasonable request.

Keywords

3D Hall sensor, deep learning model, force-measuring sensor, magnetorheological elastomer, robotic grippers, soft tactile sensors

Received: April 8, 2024

Revised: May 18, 2024

Published online: June 27, 2024

- [1] M. Costanzo, G. De Maria, C. Natale, *Front. Robot. AI* **2021**, 8 672995.
- [2] I. Huang, R. Bajcsy, *High Resolution Soft Tactile Interface for Physical Human-Robot Interaction* **2020**, pp. 1705–1711.
- [3] M. Fritzsche, N. Elkmann, E. Schulenburg, *Tactile Sensing: A Key Technology for Safe Physical Human Robot Interaction* **2011**, pp. 139–140.
- [4] J. Cao, X. Liu, J. Qiu, Z. Yue, Y. Li, Q. Xu, Y. Chen, J. Chen, H. Cheng, G. Xing, E. Song, M. Wang, Q. Liu, M. Liu, *Nat. Commun.* **2024**, 15, 1116.
- [5] J. Wu, H. Wang, Z. Su, M. Zhang, X. Hu, Y. Wang, Z. Wang, B. Zhong, W. Zhou, J. Liu, S. G. Xing, *ACS Appl. Mater. Interfaces* **2017**, 9, 38745.
- [6] Q. Hong, T. Liu, X. Guo, Z. Yan, W. Li, L. Liu, D. Wang, W. Hong, Z. Qian, A. Zhang, Z. Wang, X. Li, D. Wang, Z. Mai, Y. Zhao, F. Yan, G. Xing, *Sens. Actuators B Chem.* **2024**, 404, 135255.
- [7] S. Dong, W. Yuan, E. H. Adelson, in *2017 IEEE/RSJ Int. Conf. on Intelligent Robots and Systems (IROS)*, IEEE, Piscataway, NJ **2017**, pp. 137–144, ISBN 1538626829.
- [8] A. Alspach, K. Hashimoto, N. Kuppaswamy, R. Tedrake, in *2019 2nd IEEE Int. Conf. on Soft Robotics (RoboSoft)*, IEEE, Piscataway, NJ **2019**, pp. 597–604, ISBN 1538692600.
- [9] R. Li, et al., *Ph.D. Thesis*, Massachusetts Institute of Technology **2015**.
- [10] K. Kim, J. Ahn, Y. Jeong, J. Choi, O. Gul, I. Park, *Micro Nano Syst. Lett.* **2021**, 9, 1.
- [11] J. Morrow, H.-S. Shin, C. Phillips-Grafflin, S.-H. Jang, J. Torrey, R. Larkins, S. Dang, Y.-L. Park, D. Berenson, in *2016 IEEE Int. Conf. on Robotics and Automation (ICRA)*, IEEE, Piscataway, NJ **2016** pp. 5024–5031, ISBN 1467380261.
- [12] X. Guo, W. Hong, L. Liu, D. Wang, L. Xiang, Z. Mai, G. Tang, S. Shao, C. Jin, Q. Hong, et al., *ACS Appl. Nano Mater.* **2022**, 5, 11028.
- [13] O. Gul, K. Kim, J. Gu, J. Choi, D. Del Orbe Henriquez, J. Ahn, I. Park, *ACS Appl. Electron. Mater.* **2021**, 3, 4027.
- [14] L. Zhang, M. Gao, R. Wang, Z. Deng, L. Gui, *Sensors* **2019**, 19, 1316.
- [15] Y. Wang, M. Kamezaki, Q. Wang, H. Sakamoto, S. Sugano, in *2022 IEEE/ASME International Conf. on Advanced Intelligent Mechatronics (AIM)*, IEEE, Piscataway, NJ **2022**, pp. 302–307.
- [16] H. Mirzanejad, M. Agheli, *Sens. Actuators A: Phys.* **2019**, 293, 108.
- [17] D. S. Chathuranga, Z. Wang, Y. Noh, T. Nanayakkara, S. Hirai, in *2015 37th Annual Int. Conf. of the IEEE Engineering in Medicine and Biology Society (EMBC)*, August **2015**, pp. 5521–5524, ISSN: 1558-4615.
- [18] H. Wang, G. De Boer, J. Kow, A. Alazmani, M. Ghajari, R. Hewson, P. Culmer, *Sensors* **2016**, 16, 9.
- [19] D. S. Chathuranga, Z. Wang, Y. Noh, T. Nanayakkara, S. Hirai, *IEEE Sens. J.* **2016**, 16, 5298.
- [20] R. Bhirangi, T. Hellebrekers, C. Majidi, A. Gupta (Preprint), arXiv:2111.00071, v1, submitted: Feb. **2021**.
- [21] L. Weerasinghe, D. S. Chathuranga, in *2018 Moratuwa Engineering Research Conf. (MERCOn)*, IEEE, Piscataway, NJ **2018** pp. 102–107.
- [22] K. Wang, Y. Zhang, G. Xiao, *Phys. Rev. Appl.* **2020**, 13, 064009.
- [23] W. Othman, Z.-H. A. Lai, C. Abril, J. S. Barajas-Gamboa, R. Corcelles, M. Kroh, M. A. Qasaimeh, *Front. Robot. AI* **2022**, 8, 705662.
- [24] Y.-L. He, Z.-Q. Geng, Q.-X. Zhu, *Chem. Eng. Res. Des.* **2015**, 102, 1.
- [25] S. L. Liu, H. Cai, C. Liu, *IEEE Access* **2021**, 9, 128460.
- [26] D. S. Chathuranga, Z. Wang, Y. Noh, T. Nanayakkara, S. Hirai, in *2016 IEEE/RSJ Int. Conf. on Intelligent Robots and Systems (IROS)*, IEEE, Piscataway, NJ **2016**, pp. 5556–5563, ISSN 2153-0866.
- [27] L. Jamone, L. Natale, G. Metta, G. Sandini, *IEEE Sens. J.* **2015**, 15, 4226.
- [28] T. Paulino, P. Ribeiro, M. Neto, S. Cardoso, A. Schmitz, J. Santos-Victor, A. Bernardino, L. Jamone, in *2017 IEEE Int. Conf. on Robotics and Automation (ICRA)*, IEEE, Piscataway, NJ **2017**, pp. 966–971.
- [29] T. Kim, S. Lee, T. Hong, G. Shin, T. Kim, Y.-L. Park, *Sci. Robot.* **2020**, 5, eabc6878.
- [30] U. Sharif, B. Sun, S. Hussain, D. S. Ibrahim, O. O. Adewale, S. Ashraf, F. Bashir, *Mater.* **2021**, 14, 7025.
- [31] H. Böse, *Int. J. Mod. Phys. B* **2007**, 21, 28n29 4790.
- [32] C. Ruddy, E. Ahearne, G. Byrne, *Adv. Manuf. Sci. Res.* **2012**, 20, 53319553.
- [33] J. D. Carlson, M. R. Jolly, *Mechatronics* **2000**, 10, 555.
- [34] M. Lokander, B. Stenberg, *Polym. Test.* **2003**, 22, 245.
- [35] T. Kawasetsu, T. Horii, H. Ishihara, M. Asada, *Sensors* **2018**, 18, 2.
- [36] M. A. Khalid, M. M. Saleem, S. A. R. Bukhari, M. I. Tiwana, R. I. Shakoob, R. Cheung, *IEEE Sens. J.* **2023**, 23, 247.
- [37] H. Fu, Y. Jiang, J. Lv, Y. Huang, Z. Gai, Y. Liu, P. S. Lee, H. Xu, D. Wu, *Adv. Sci.* **2023**, 10, 2206094.
- [38] X.-Y. Li, P.-P. Zhao, L.-X. Han, C. Deng, *Compos. Sci. Technol.* **2022**, 219, 109221.
- [39] G. Heo, K.-H. Pyo, D. H. Lee, Y. Kim, J.-W. Kim, *Sci. Rep.* **2016**, 6, 25358.
- [40] M. Park, T. Park, Y. L. Park, *Extreme Mech. Lett.* **2023**, 60, 101983.
- [41] *Onrobot, Datasheet: SG Base Part AD SG Silicone Tools*, **2021**.
- [42] Y. Wu, Y. Liu, Y. Zhou, Q. Man, C. Hu, W. Asghar, F. Li, Z. Yu, J. Shang, G. Liu, *Sci. Robot.* **2018**, 3, eaat0429.
- [43] Y. Yan, Z. Hu, Z. Yang, W. Yuan, C. Song, J. Pan, Y. Shen, *Sci. Robot.* **2021**, 6, eabc8801.
- [44] X. Hu, H. Zhu, R. Chen, S. Hu, Z. Jia, H. Yu, S. Qu, *Adv. Intell. Syst.* **2023**, 5, 2200291.
- [45] A. Mohammadi, Y. Xu, Y. Tan, P. Choong, D. Oetomo, *Sensors* **2019**, 19, 4925.
- [46] G. De Boer, N. Raske, H. Wang, J. Kow, A. Alazmani, M. Ghajari, P. Culmer, R. Hewson, *Sensors* **2017**, 17, 2539.
- [47] A. Fessel, H.-G. Döbereiner, *Biomech. Model. Mechanobiol.* **2018**, 17, 419.
- [48] W. Zhang, X. Gong, W. Jiang, Y. Fan, *Smart Mater. Struct.* **2010**, 19, 085008.
- [49] M. A. Tasin, S. A. A. Aziz, S. A. Mazlan, M. A. F. Johari, N. A. Nordin, S. Y. M. Yusuf, S.-B. Choi, I. Bahiuddin, *Micromachines* **2023**, 14, 767.
- [50] C. Wu, C. Cheng, A. Abd El-Aty, T. Li, Y. Qin, Q. Yang, S. Hu, Y. Xu, X. Guo, *Mater. Res. Express* **2020**, 7, 086101.
- [51] H. Song, N. Wereley, R. Bell, J. Planinsek, J. Filer II, *J. Phys. Conf. Ser.* **2009**, 149, 012097.
- [52] W. Zhang, X. Gong, S. Xuan, W. Jiang, *Ind. Eng. Chem. Res.* **2011**, 50, 6704.
- [53] Y. Zhou, S. Jerrams, A. Betts, L. Chen, *Mater. Chem. Phys.* **2014**, 146, 487.
- [54] W. Li, Y. Zhou, T. Tian, *Rheol. Acta* **2010**, 49, 733.
- [55] M. Cvek, R. Moucka, M. Sedlacik, V. Pavlinek, *Smart Mater. Struct.* **2017**, 26, 105003.
- [56] D. Gorman, N. Murphy, R. Ekins, S. Jerrams, *Int. J. Fatigue* **2017**, 103, 1.
- [57] Y. Zhou, S. Jerrams, A. Betts, G. Farrell, L. Chen, *Mater. Des.* **2015**, 67, 398.
- [58] D. Gorman, N. Murphy, R. Ekins, S. Jerrams, *Polym. Test.* **2016**, 51, 74.

- [59] Y. Zhou, L. Jiang, S. Chen, J. Ma, A. Betts, S. Jerrams, *Polym. Test.* **2017**, 61, 177.
- [60] A. K. Bastola, M. Hossain, *Compos. B: Eng.* **2020**, 200, 108348.
- [61] R. J. Wolf, L. Hedeon, *Temperature Stable Proximity Sensor with Sensing of Flux Emanating from the Lateral Surface of a Magnet* **1990**.
- [62] T. Komatsuzaki, T. Inoue, O. Terashima, *Mechatronics* **2016**, 40, 128.
- [63] S. W. Chen, R. Li, Z. Zhang, X. J. Wang, *Smart Mater. Struct.* **2016**, 25, 035001.
- [64] X. Dong, in *Smart And Functional Soft Materials*, IntechOpen, London, England **2019**.
- [65] R. K. Shuib, K. L. Pickering, B. R. Mace, *J. Appl. Polym. Sci.* **2015**, 132.
- [66] J. Saleem, A. Majid, K. Bertilsson, L. Schuberg, in *2011 10th Int. Conf. on Environment and Electrical Engineering*, IEEE, Piscataway, NJ **2011**, pp. 1–4.
- [67] S.-M. Yang, Y.-C. Chang, in *IECON 2007-33rd Annual Conf. of the IEEE Industrial Electronics Society*, IEEE, Piscataway, NJ **2007** pp. 2225–2229.
- [68] G. Y. Zhou, *Smart Mater. Struct.* **2003**, 12, 139.
- [69] X. G. Huang, Z. Y. Yan, C. Liu, G. H. Li, J. Wang, *Mater. Res. Innov.* **2015**, 19, S5.
- [70] Z. Ying, Y. Ni, M. Sajjadi, *Sci. China Technol. Sci.* **2013**, 56, 878.
- [71] A. Dorfmann, R. Ogden, *Acta Mech.* **2004**, 167, 13.
- [72] R. Bustamante, *Acta Mech.* **2010**, 210, 183.
- [73] J. M. Ginder, M. E. Nichols, L. D. Elie, J. L. Tardiff, in *1999 Symp. on Smart Structures and Materials*, Vol. 3675, SPIE, **1999**, pp. 131–138.
- [74] G. Y. Zhou, J. R. Li, *Smart Mater. Struct.* **2003**, 12, 859.
- [75] T. K. Kim, J. K. Kim, O. C. Jeong, *Microelectron. Eng.* **2011**, 88, 1982.
- [76] W. S. Lee, K. S. Yeo, A. Andriyana, Y. G. Shee, F. R. M. Adikan, *Mater. Des.* **2016**, 96, 470.
- [77] A. Thorin, A. Azoug, A. Constantinescu, *Polym. Test.* **2012**, 31, 978.
- [78] Y. Zhang, F. Fang, W. Huang, Y. Chen, S. Qi, M. Yu, *Front. Mater.* **2019**, 6.
- [79] M. Trebar, Z. Susteric, U. Lotric, *Polymer* **2007**, 48, 5340.
- [80] H. A. Sonar, M. C. Yuen, R. Kramer-Bottiglio, J. Paik, in *2018 IEEE Int. Conf. on Soft Robotics (RoboSoft)*, IEEE, Piscataway, NJ **2018**, pp. 170–175.
- [81] W. Navaraj, R. Dahiya, *Adv. Intell. Syst.* **2019**, 1, 1900051.
- [82] S. Sundaram, P. Kellnhofer, Y. Li, J.-Y. Zhu, A. Torralba, W. Matusik, *Nature* **2019**, 569, 698.
- [83] M. Krautz, D. Werner, M. Schrödner, A. Funk, A. Jantz, J. Popp, J. Eckert, A. Waske, *J. Magn. Magn. Mater.* **2017**, 426, 60.
- [84] Y. Yu, Y. Li, J. Li, X. Gu, *Smart Mater. Struct.* **2016**, 25, 055029.
- [85] J. S. Bergstrom, in *Mechanics Of Solid Polymers: Theory And Computational Modeling*, William Andrew, Norwich, NY **2015**.
- [86] T. Windeatt, *IEEE Trans. Neural Networks* **2006**, 17, 1194.
- [87] I. Yilmaz, O. Kaynar, *Expert Syst. Appl.* **2011**, 38, 5958.
- [88] M. Subramaniyan, A. Skoogh, J. Bokrantz, M. A. Sheikh, M. Thürer, Q. Chang, *J. Manuf. Syst.* **2021**, 60, 734.
- [89] Y. Zhang, A. S. Sezen, R. Rajamani, *IEEE Sens. J.* **2020**, 21, 239.
- [90] T. Yao, X. Guo, C. Li, H. Qi, H. Lin, L. Liu, Y. Dai, L. Qu, Z. Huang, P. Liu, *J. Phys. D: Appl. Phys.* **2020**, 53, 445109.
- [91] V. Kakani, X. Cui, M. Ma, H. Kim, *Sensors* **2021**, 21, 1920.